



IFIN-HH



UPB



ELI-NP

UNIVERSITY POLITEHNICA of BUCHAREST

Doctoral School in Engineering and Applications of Lasers and Accelerators

Doctoral Thesis

Summary

Methods for characterization of particle pulses generated by high power
laser interaction with matter

Author: Lucian Tudor

Supervisor: CS1 Dr. Călin A. Ur

Bucharest 2020

Contents

Nomenclature	iii
Introduction	1
1 Proton and heavy ions acceleration mechanisms using solid targets. Basic principles	
1.1 Basics of Laser-Plasma Interaction.....	3
1.2 Ion acceleration mechanisms.....	3
1.2.1 Target Normal Sheath Acceleration (TNSA).....	4
1.2.2 Radiation Pressure Acceleration (RPA).....	5
2 Detection and characterization of charged particles pulses resulting from the interaction of lasers with solid targets	
2.1 Thomson Parabola Spectrometer.....	7
2.1.1 Conceptual Design for E1 Thomson Parabola spectrometer.....	8
2.1.1.1 Analytical calculation methods and SIMION simulations.....	9
2.1.1.2 Thomson parabola theoretical resolution.....	10
2.1.2 Conceptual Design for E5 Thomson Parabola spectrometer.....	10
2.1.2.1 E5 Thomson Parabola configuration 1.....	10
2.1.2.2 E5 Thomson Parabola configuration 2.....	11
2.1.3 Detection screen and signal estimation.....	11
2.1.4 Technical design.....	12
2.1.5 Conclusions.....	13
2.2 Radiochromic films calibration for protons at 9 MV Tandem accelerator.....	14
2.2.1 Experimental setup.....	14
2.2.2 Data analysis.....	15
2.2.2.1 Sources of uncertainty.....	16
2.2.2.2 Results and discussion.....	16
2.2.3 Proton characterization in LASER acceleration experiments.....	16
2.2.4 Conclusions.....	17

3	Proton diagnostics based on population and de-excitation of nuclear isomeric states - gamma spectroscopy	
	3.1 Method description.....	19
	3.2 Tests and experimental set-up.....	20
	3.2.1 Detection system - description and characterization.....	20
	3.2.2 Selection of the secondary targets.....	21
	3.2.3 Experimental set-up.....	21
	3.3 Measured γ -ray energy spectra - preliminary results.....	22
	3.4 Proton beam characterization.....	27
	3.4.1 Calculation of the reaction number.....	27
	3.4.2 Determination of incident projectile number.....	27
	3.5 Detector recovery time.....	29
	3.6 Conclusions.....	30
4	Outlook and perspectives.....	31
	References	35
	Peer reviewed publications	39

Nomenclature

ASE	amplified spontaneous emission
CCD	charge coupled device
CE	Coulomb explosion
EMP	electromagnetic pulse
HB	hole boring
HPLS	high power laser system
IP	image plate
IT	isomeric transition
LS	light sail
NAIS	nuclear activation-based imaging spectroscopy
OAA	off-axis angle
OAP	off-axis parabolic mirror
OD	optical density
OFB	optical fiber bundle
PMT	photomultiplier tube
RCF	radiochromic films
RF	radiofrequency
RPA	radiation pressure acceleration
S/N	signal-to-noise ratio
TNSA	target normal sheath acceleration
TP	Thomson parabola

Introduction

In the last decades, high-power lasers (Terrawatt, Petawatt) have begun to present a growing interest in fundamental nuclear physics and applied sciences, being able to produce high energy charged particles, such as GeV ions [1], electrons and protons with energies up to near 100 MeV [2, 3], high flux neutrons [4], generated directly in a primary target via (d,d) or (d,t) [5] reactions or using a secondary target via (p,n), (d,n) [4, 6, 7] or photonuclear reactions [8] as well as high energy X and gamma radiation obtained using bremsstrahlung [9], betatron [10] or inverse-Compton scattering [11] mechanisms. Compared with classical radiofrequency particle accelerators, high power lasers can provide unique characteristics of accelerated particles such as several types of particles accelerated simultaneously in high density short duration bunches. These features make high-power lasers a great tool for therapy and diagnostic applications in nuclear medicine [12], space science and material technology [13], fundamental nuclear physics [8], fusion fast ignition [14], etc.

The Extreme Light Infrastructure (ELI) project promises to push the boundaries of knowledge in this area beyond what has been achieved so far. ELI consists in three pillars: ELI – Beamlines (in Czech Republic), ELI - Attosecond (in Hungary) and ELI - Nuclear Physics (in Romania). ELI-Nuclear Physics (ELI-NP) is the most powerful laser infrastructure built so far, and it will consist of two components. The first component is a high power laser system consisting of two amplifying lines that will work in parallel, each amplifier line having three outputs with different maximum powers: 10 PW with a repetition rate of 0.017 Hz, capable of reaching laser intensities of more than 10^{22} W/cm² and electric fields above 10^{15} V/m, 1 PW with 1 Hz repetition rate, 100 TW with a repetition rate of 10 Hz. The second ELI-NP component will be a system that can generate a very intense gamma beam with energy continuously tunable between 1 MeV and 19.5 MeV, relative bandwidth better than 0.5% and a spectral density higher than 0.5×10^4 photons/s/eV, which is obtained by laser inverse Compton scattering off relativistic electron bunches [15].

The work presented in this thesis is addressing the problem of nuclear diagnostics required by high power laser experiments at ELI-NP. In order to measure and characterize accelerated particles at ELI-NP, we need to develop an optimized generation of detectors, which are able to determine with high resolution the particle energy, mass to charge state, particle beam intensity and distribution.

The thesis is divided into three chapters, the first one gives an introduction into the basic principles of the proton and heavy ion acceleration mechanisms using solid targets: Target Normal

Sheath Acceleration (TNSA) and Radiation Pressure Acceleration (RPA), and underlines the main characteristics of the particle beams accelerated using these mechanisms.

The second chapter has two major parts. First part describes three extended range Thomson Parabola spectrometers, designed to measure protons with energies ranging from 1 MeV to 200 MeV and carbon ions with energies ranging from 1 MeV/n to 160 MeV/n resulting from the high power laser interaction with matter. The second part of the chapter describes a calibration experiment of Radiochromic films, which will be used for dose, energy and beam profile characterisation of the high power laser accelerated particles at ELI-NP.

The third chapter contains an in-detail description of an experiment which was done to test and optimize a method for characterization of high power laser accelerated proton pulses based on the production in secondary targets of nuclear isomers and in-situ measurement of the γ de-excitation of reaction products using LaBr₃:Ce scintillators.

In the last part are summarized the conclusions of the thesis and are presented the future plans for contributing to R&D of methods and detectors for characterization of particle pulses generated by high power laser interaction with solid targets at ELI-NP.

Chapter 1

Proton and heavy ions acceleration mechanisms using solid targets. Basic principles

In the following we will present the most important high power laser ion acceleration mechanisms and the main properties of generated particles that define the properties of diagnostics developed for their characterisation in terms of energies, angular coverage, sensibility and resolution.

1.1 Basics of Laser-Plasma Interaction

The motion of a single electron with mass m_e and negative electric charge e in the presence of electromagnetic fields \mathbf{E} and \mathbf{B} is described by Lorentz equation [16]:

$$\frac{d\mathbf{p}}{dt} = -e(\mathbf{E} + \mathbf{v} \times \mathbf{B}) \quad (1)$$

implying, after multiplication with \mathbf{v} , the energy equation:

$$\frac{d}{dt}(\gamma m_e c^2) = -e(\mathbf{v} \cdot \mathbf{E}) \quad (2)$$

where \mathbf{v} is the velocity of the electron, $\mathbf{p} = \gamma m_e \mathbf{v}$ is the momentum of the electron, c is the light speed in vacuum and γ is the relativistic factor:

$$\gamma = \left(1 + \frac{p^2}{m_e^2 c^2}\right)^{\frac{1}{2}} = \left(1 - \frac{v^2}{c^2}\right)^{-\frac{1}{2}} \quad (3)$$

In these formulae the quantities appearing in bold-italics are 3 dimensional vectors and those only in italics are modulus of the 3D vectors or other scalar quantities.

Inside plasma, the negative charge of electrons is compensated by positive atomic nuclei. A displacement $d\mathbf{r}$ of electrons in a $dV = dSdl$ volume will generate a region of net positive charge $Q = e n_e dSdr$ as well as a region of equal negative charge establishing across the displaced volume a uniform field $E = \frac{Q}{dS} / \epsilon_0 = e n_e dr / \epsilon_0$ in $d\mathbf{r}$ direction (using plane capacitor formula).

1.2 Ion acceleration mechanisms

In the last decades, several ion acceleration mechanisms were identified, two of the most important are Target Normal Sheath Acceleration (TNSA) and Radiation Pressure Acceleration (RPA).

In Figure 1.1, based on the main parameters of the laser pulse and the target, an overview of acceleration regimes is presented [20].

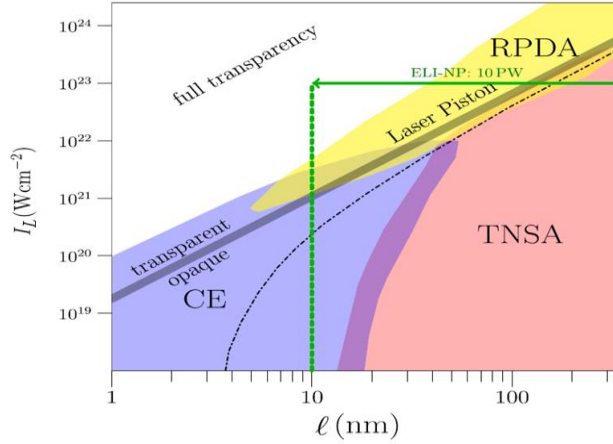


Figure 1.1: Regimes of laser-driven ion acceleration with target normal sheath acceleration (TNSA), radiation-pressure-dominated acceleration (RPDA) and Coulomb explosion (CE). The gray line indicates the opaque/transparent border and the dashed line the target thickness ℓ for which the proton energy at a given laser intensity I_L will be maximal. The regimes overlap in certain parameter regions. Intensity conditions, as indicated by the green arrow, should be reachable with the ELI-NP 10 PW HPLS [20].

1.2.1 Target Normal Sheath Acceleration (TNSA)

TNSA is the dominant mechanism for laser-driven proton acceleration in most experiments reported till now, for both “long” and “short” laser pulses [17]. The TNSA mechanism has been described since 2001 [19] and it is based on an efficient generation of hot electrons in relativistic regime, that after reaching the rear side of the target, form a sheath region. This sheath at the rear side of the target generates a high space-charge electric field with a back-holding effect for the hot electrons, the electric potential drop through the sheath being [18]:

$$\Delta\phi \approx T_f/e \quad (4)$$

where the T_f is the fast electron temperature.

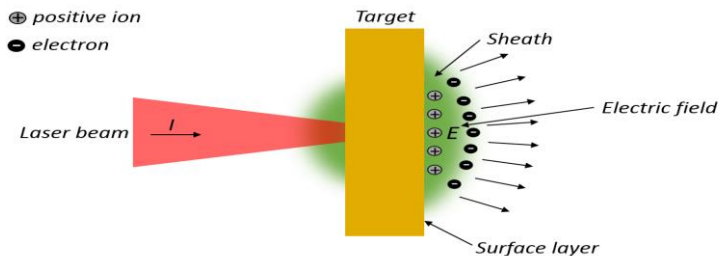


Figure 1.2: Schematic description of Target Normal Sheath Acceleration (TNSA) mechanism. The laser beam hits the front side of the target and pushes the electrons to the back side of the target, forming a sheath region. A high space-charge electric field with a back-holding effect for the hot electrons is created and it accelerates ions perpendicular to the target surface.

In this mechanism, the electric field at the rear side of the target accelerate ions perpendicular to the target surface (normal to the target).

TNSA regime can be easily reached by using a laser pulse with $I_L \geq 10^{18} \text{ W/cm}^2$ and targets of tens of nm thicknesses [20]. The TNSA proton energy spectrum is typically broad (starting from energies of few keV to a cutoff energy) with a large angular distribution of $\sim 45^\circ$. The particle number per MeV has an exponential distribution with a sharp cutoff at the maximum energy. Till now, the maximum reported proton energy obtained by using TNSA acceleration mechanism is $\sim 70 \text{ MeV}$, with a number of protons per MeV ranging from $\sim 10^{12}$ (at low energies) to $\sim 10^7$ (at maximum energy) [21]. Usually the TNSA accelerated ion beam has a short time duration (ns).

1.2.2 Radiation Pressure Acceleration (RPA)

In the RPA mechanism, when an electromagnetic wave hits a flat target the electromagnetic wave momentum is transferred to the target, producing pressure. The pressure for a monochromatic electromagnetic wave with intensity I , perpendicular on the plane target at rest is given by [18]:

$$P_{rad} = (1 + \mathcal{R} - \mathcal{T})\frac{I}{c} = (2\mathcal{R} + \mathcal{A})\frac{I}{c} \quad (5)$$

where \mathcal{A} , \mathcal{R} and \mathcal{T} are the absorption, reflection and transmission coefficient (conservation of energy impose the constraint $\mathcal{R} + \mathcal{T} = 1 - \mathcal{A}$). The maximum pressure $P_{rad} = 2I/c$ can be obtained in case of an ideal mirror with $\mathcal{R} = 1$ and $\mathcal{T} = \mathcal{A} = 0$.

Hole boring regime (interaction of laser pulse with thick targets)

In the hole boring (HB) regime, the intense pressure of a laser pushes the surface of an overdense plasma towards the target interior, thus increasing plasma density in that region and leading to recession on the interaction surface. In multi-dimensional geometry, the action of radiation pressure bores a hole in the plasma, the surface velocity is commonly called “hole boring” (HB) velocity v_{HB} .

Light sail regime (interaction of laser pulse with thin targets)

If thin targets are used, with $l \ll v_{HB}\tau_p$, where l is the target thickness and τ_p is the laser pulse duration, the HB front reaches the rear side of the target before the laser pulse duration ends, then the whole mass of the target is accelerated [18]. In this case the ions are accelerated with higher velocities than in the HB regime, whereas the ions are not anymore screened by a background plasma [17]. This regime can be associated, in a simplistic form, to a thin mirror boosted by RPA, like a “light sail” (LS).

To reach the RPA regime the laser parameters requirements are higher as compared to the TNSA regime. The laser pulse intensities I_L needs to be $\geq 10^{21} \text{ W/cm}^2$ if very thin targets $\sim 10 \text{ nm}$ are used, and it needs to be even higher if thicker targets (teens of nm) are used [20]. As compared to

TNSA, the RPA regime has a higher conversion efficiency and the energy spectrum is typically quasi-monoenergetic [22], with a typically angular distribution below $\sim 30^\circ$. Up to now, pure RPA has not been obtained experimentally, but a RPA-TNSA hybrid regime was produced. The maximum energy of the protons accelerated by using RPA-dominant mechanism, reported till now, is ~ 100 MeV, with a number of protons ($MeV^{-1}Sr^{-1}$) ranging from 10^{12} (at low energies) to 10^9 (at maximum energy) [3]. In case of RPA regime, the ion beam pulse duration is shorter as compared to the TNSA regime, being usually in the order of ps.

Chapter 2

Detection and characterization of charged particles pulses resulting from the interaction of lasers with solid targets

In the last years, remarkable progress occurred in the field of laser-matter interaction, many laboratories reporting production of high energy charged particles, such as GeV ions [1] and protons with energies up to near 100 MeV [2, 3]. The Extreme Light Infrastructure - Nuclear Physics (ELI-NP) hosts the most powerful lasers in the world (10 Peta Watts) and promises to push the boundaries of knowledge in this area beyond what has been achieved so far. The interaction of ultra-high power laser with solid targets will produce in the same time different types of high energy charged particles (protons, ions and electrons) and very high intensity electromagnetic fields, ranging from the radiofrequency and Terra Hertz range to the X-ray and γ ranges [8].

To measure and characterize accelerated particles at ELI-NP, an optimized generation of detectors for working with particles produced in interactions of ultra-high intensity lasers (immune to electromagnetic pulses), needs to be developed in order to determine with high resolution the particle energy, mass to charge state ratio, particle beam intensity and distribution.

This chapter presents two important tools in laser-driven accelerated particles measurements, both immune to the electromagnetic pulses. In the first part of the chapter are described three extended range Thomson Parabola (TP) spectrometers, able to measure at ELI-NP protons with energies ranging from 1 MeV to 200 MeV and carbon ions with energies ranging from 1 MeV/n to 160 MeV/n. Following that, in the second chapter the calibration experiment of Radiochromic Films (RCF), which will be used for dose, energy and beam profile characterisation of the high power laser accelerated particles at ELI-NP is discussed.

2.1 Thomson Parabola Spectrometer

Thomson Parabola (TP) spectrometers are an important diagnostic tool in particle acceleration experiments using high-power lasers [23, 24]. The TP spectrometer idea was mentioned first time in 1911, by J.J. Thomson [25]. TP spectrometer is able to measure, in a given solid angle, the energy distribution and particles type (based on mass to charge ratio) of accelerated protons and ions resulting

from the interaction of high power laser beams with matter in the TW to PW regime, based on the particles deflection in magnetic and electric fields [20, 26, 27].

Until now the TP spectrometers were designed in many different configurations [28, 29, 30, 31], taking into account the new LASER features that will be capable of delivering powers up to 10 PW [32], the development of TP spectrometers capable of measuring high energy ions is required. In this chapter the design of extended range TP spectrometers is presented. The TP spectrometers configurations discussed in this thesis are designed to be used for characterisation of accelerated ions at E1 experimental area of ELI-NP, where 10 PW laser beam will be used for Laser Driven Nuclear Physics experiments [8], and at E5 experimental area where the 1 PW laser beam [33] will be used for radiation hardness testing in extreme conditions (ex. Cosmic space) of materials and biological probes [13]. The designs are based on analytical calculations and simulations made with SIMION v7 code [34], a specific software for charged particle trajectory simulations. In the presented configurations the TP spectrometers are able to measure the energy spectra of proton and carbon ions, with high resolution, on a shot by shot basis. Simulations were performed for protons in an energy range from 1 MeV to 200 MeV and carbon ions in an energy range from 1 MeV/n to 160 MeV/n. The TP spectrometer measures only a small part of particle emission due to the low angular acceptance (0.2 mrad) but it has a large acceptance in terms of energy, and it is immune to electromagnetic pulses (EMP) [35, 36] when coupled to passive detectors [37].

2.1.1 Conceptual Design for E1 Thomson Parabola spectrometer

The maximum expected energy for accelerated protons in E1 experimental area is up to 200 MeV, the E1 TP design is optimized to measure with high resolution protons with energies up to 200 MeV. The simplified scheme of the E1 TP can be observed in Figure 2.1. As a detector screen we plan to use two major types of detectors, active and passive. For the passive detection we will use Image Plates [IP] [38, 39] and CR 39 [40, 41], while for active detection we will use scintillation screens (LANEX screens [42] and plastic scintillators) coupled to CCD cameras.

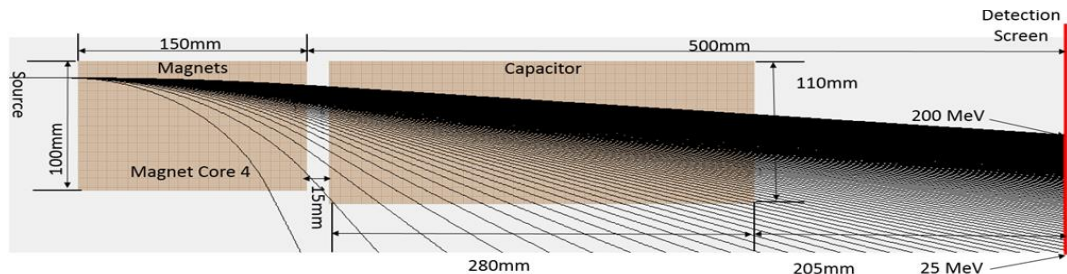


Figure 2.1: Side view of the E1 TP spectrometer placed along the beam initial propagation direction. The E1 TP consist in a 200 μm pinhole with a length of 30 mm, a 150 x 100 mm^2 permanent magnetic core with a gap of 10 mm (with the centre aligned to the beam axis, 1 T magnetic field), a 280 x 110 mm^2 capacitor with a gap of 10 mm (with the centre shifted 3 mm to the left of the beam axis, 26 kV applied voltage) placed at 15 mm distance from the magnetic core, and a 100 x 50 mm^2 detection screen placed at 205 mm distance from the capacitor.

2.1.1.1 Analytical calculation methods and SIMION simulations

The proton and ions trajectories (after passing through magnetic and electric field) were calculated by using two methods. In a first step were used analytical formulas, under assumption of classical [43] and relativistic particles kinematics. In the second step the simulations were performed by using the SIMION V7 code. The analytical calculations and SIMION simulations are based on the same input values, given by the E1 TP configuration.

The results obtained from analytical calculation using classical kinematics were compared with the results obtained using SIMION simulation (for deflection in magnetic field). It was observed a proportional dependence between the deviation of the analytical curve with respect to the SIMION curve and the proton energy, ranging from 1.49% at 60MeV to 5.89% at 200 MeV. For a better overlap between the analytical calculation and SIMION simulation deflection curves we have to take into account the relativistic particle kinematics. The analytical calculations, under assumption of relativistic kinematics [44], offer a relative difference to the SIMION simulation curve under 0.31%, increasing the accuracy of the analytical calculations by at least one order of magnitude when compared to the results obtained in the classical case.

The deflection in electric field become very important when several types of particles (e.g. protons and ions) are measured at the same time. The magnetic field changes the particles position on the Oz axis, which does not allow us to identify what type of particles are deflected at different positions on the Oz axis. To change the particle position also on the Oy axis, one needs to introduce the electric field. By using both magnetic and electric fields, the deflected particles (with distinct mass to charge ratio), measured in the detection screen plane, form parabolic traces (see Figure 2.2).

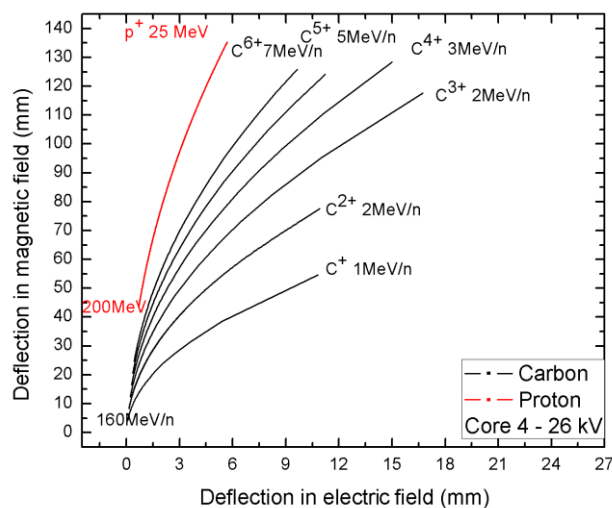


Figure 2.2: Proton (red line) and carbon ion (black line) deflection in the detection plane after passage through the magnetic ($B_{max} = 1$ T) and electric field $U_{max} = 26$ kV, in E1 TP spectrometer configuration.

2.1.1.2 Thomson parabola theoretical resolution

Assuming a Gaussian distribution, the resolution is defined as the full width at half maximum (FWHM) of the variance of the spectrometer energy distribution Δ_E response for incoming monoenergetic ions divided by the energy E_0 (Δ_E/E_0 at FWHM). To determine the resolution, a conical ion beam spatially filtered by a 200 μm pinhole was used.

The results of the calculations by using the E1 TP spectrometer configuration, show that the theoretical energy resolution is under 1.5% for protons with energy of 200 MeV and under 2% for C^{6+} ions of 160 MeV/n.

2.1.2 Conceptual Design for E5 Thomson Parabola spectrometer

The E5 TP spectrometers designs are optimized to measure with high resolution protons with energies up to 100 MeV that is the maximum expected proton energy. The general conceptual scheme remain the same like in Chapter 2.1.1 but for E5 experimental area we will use two TP spectrometer configurations, configuration 1 designed to measure protons with energy in the range between 1 MeV and 50 MeV and configuration 2 designed to measure protons with energy in the range between 3 MeV and 100 MeV.

2.1.2.1 E5 Thomson Parabola configuration 1

The E5 TP 1 is designed to measure protons with energies up to 50 MeV. The E5 TP 1 have been characterized and calibrated (proton deflection in magnetic field) in vacuum, for protons with energies ranging from 4 MeV to 10 MeV at Horia Hulubei National Institute for Physics and Nuclear Engineering IFIN-HH 9 MV Tandem accelerator. The experimental setup is shown in Figure 2.3.

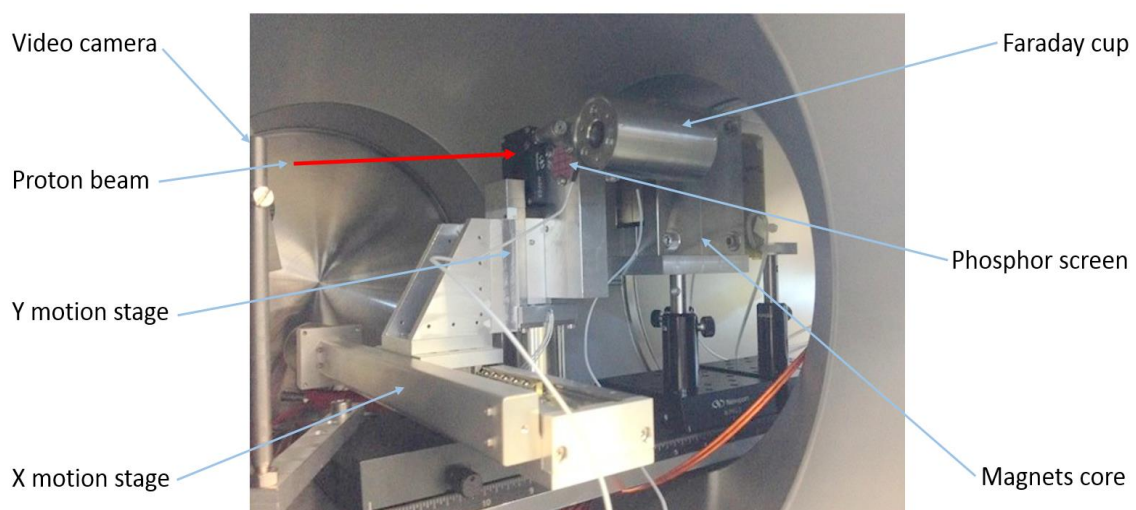


Figure 2.3: E5 TP1 spectrometer calibration experimental setup, mounted in vacuum chamber at IFIN-HH 9 MV Tandem accelerator. The proton beam comes from the left side of the picture (see red arrow).

The E5 TP 1 proton (with energies between 4 MeV to 10 MeV) deflection measured experimentally at the 9 MV Tandem accelerator was compared with the proton (with energies between 1 to 50 MeV) deflection simulated by using SIMION software (see Figure 2.4).

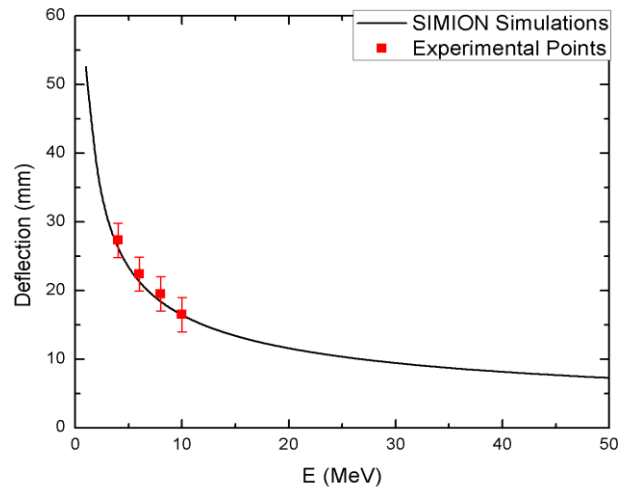


Figure 2.4: E5 TP 1 protons (from 4 MeV to 10 MeV) deflection measured experimentally at the 9 MV Tandem accelerator (red dots) vs proton (from 1 MeV to 50 MeV) deflection simulated by using SIMION software (black line).

The data analysis shows a relative difference between the proton deflection simulated by using SIMION and the experimentally measured proton deflection below 6%.

The E5 TP 1 structure together with the distributions of magnetic and electric field make the E5 TP 1 able to measure protons with the energy range between 1 MeV to 50 MeV with a theoretical energy resolution below 3%.

2.1.2.2 E5 Thomson Parabola configuration 2

The E5 TP 2 is designed to measure protons with energies up to 100 MeV. The E5 TP 2 structure together with the distributions of magnetic and electric field make the E5 TP 2 able to measure protons with energy in the range between 3 MeV and 100 MeV, with a theoretical energy resolution below 1.5% for protons with energies of 100 MeV and carbon ions, with energy in the range between 1 MeV/n and 50 MeV/n with a theoretical energy resolution below 2% for C^{6+} ions of 50 MeV/n.

2.1.3 Detection screen and signal estimation

The signal estimation is a very important part of the Thomson Parabola spectrometers development, based on the proton number distribution function of energy, for the highest energies obtained so far experimentally [3], the proper distances and pinhole diameters were chosen for each TP spectrometers, which will be placed in E1 and E5 experimental areas.

The E1 TP pinhole diameter used in simulations is 200 μm and the thickness is 30 mm, for a 1000 mm distance from target to the TP pinhole (0.2 mrad acceptance) and 750 mm distance from

pinhole entrance to detection screen, the pinhole acceptance is $3.14 \cdot 10^{-8}$ Sr, enough to have few tens (~ 30) of particles per shot in a bin of 1 MeV of protons at maximum energy. Taking into account the E5 TPs geometries, the number of particles per shot in a bin of 1 MeV of protons at maximum energy which hit the detection screen is the same as in the E1 TP case.

The Thomson Parabola spectrometers will use as detection plane two types of detectors, in the first experiments at ELI-NP, an offline detector will be used (IP) and in the future experiment online detectors will be used (LANEX screens and plastic scintillators). The signals from the online detectors will be collected and sent outside the interaction chamber by using an optical system consisting of a system of lens, an optical fiber bundle (OFB) coupled to an optical feedthrough and a PCO camera. The offline solution is already tested in many particle acceleration experiments by using high-power lasers, as a detection screen for Thomson Parabola [38, 39], so the focus will be on estimating the signal generated by the scintillators that will be used as online TP detection screen (online readout). With the estimated number of protons, approximated above, an estimation can be made of the number of photons emitted for this case. Two types of active detection screens, BC 430 plastic scintillator and LANEX fast, were compared. Taking into account the TP angular acceptance, the proton energy loss in the active volume of the scintillator (calculated with GEANT4), the light emission (photons/MeV) of the scintillators (BC 430 [45] and LANEX [46]), and the system used to collect the light emitted (OFB [47] and PCO camera [48]), in both cases the number of emitted photons is enough to be detected properly by the PCO camera coupled to the optical system.

Signal to noise ratio estimation

The TP spectrometer will be placed in our experiments in most cases right along, or at a small angle with respect to the laser-beam axis. Hence, the TP is expected to be the instrument which is most affected by the strong and energetic γ -ray flash which emerges during any laser shot. Therefore, an estimation of the signal-to-noise ratio (S/N) for high energy proton detection is a crucial task in the design and the implementation of the instrument. For this purpose, several sets of simulations were performed with the GEANT 4 toolkit for the passage of particles and radiation through matter.

The results of the study show that the adopted shielding configuration ensures the 200 MeV protons can be detected with the instrument as, in worst case, an *S/N-ratio of 7:1* can be still assumed if one decides to use a Pb shielding with a thickness of 80 mm at the front face and 30 mm for the sides and the rear.

2.1.4 Technical design

In Figure 2.5 is presented the preliminary technical draw, without shielding, of the E1 TP spectrometer (see Chapter 2.1.1). The E1 TP spectrometer pinhole has 200 μm diameter and 30 mm length, which means it will be very difficult to align it. To be able to make such a precise alignment, the pinhole will be mounted on a kinematic support (μm precision) and we will use a laser diode

mounted in the back side of the spectrometer to check the alignment. The detection screen will be mounted on a removable support, when passive detectors will be used. After each laser pulse, the passive detector has to be quickly removed and replaced with a new one. The whole assembly of spectrometer components will be mounted in a box that will be placed on a height adjustable support, which will allow us to make the rough alignment of the spectrometer.

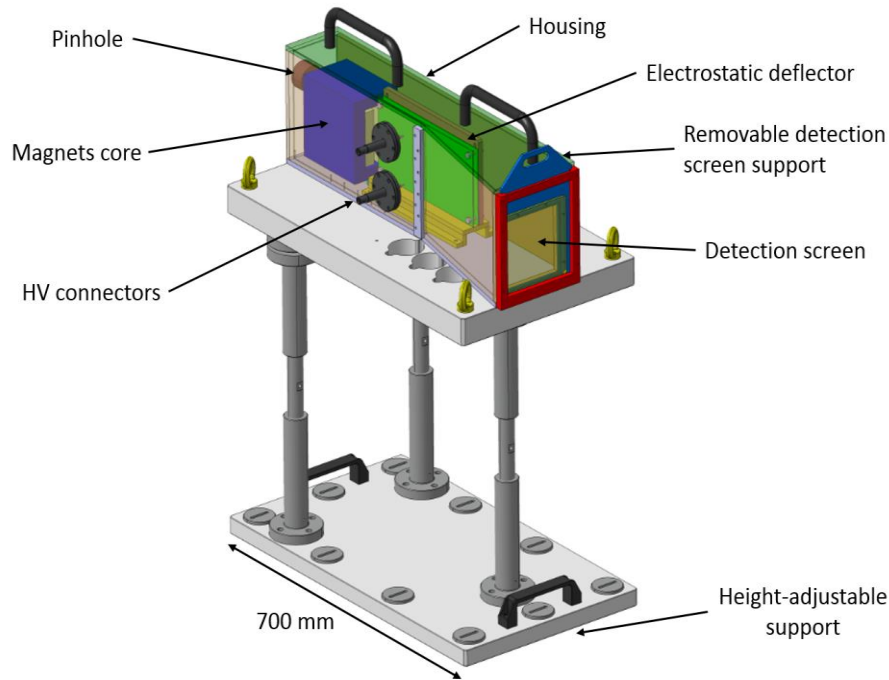


Figure 2.5: Schematic 3D isometric back view of the E1 TP spectrometer mounted on the height adjustable support. The detector has an overall length ≈ 700 mm and height ≈ 900 mm.

2.1.5 Conclusions

In this chapter a complete solution for high resolution measurements of protons with energies starting from 1 MeV up to 200 MeV and carbon ions with energies starting from 1 MeV/n up to 160 MeV/n, using different new designs of extended range Thomson Parabola spectrometers is presented. Due to the optimized Thomson Parabola spectrometer designs, the energy resolution is under 3% for protons and under 2% for C^{6+} ions, over the whole range of energy. The theoretical calculations were done with SIMION 7 ion optics software, the obtained results have been successfully compared with analytical calculation, the relative difference between the two types of calculation being only 0.31% in the best approximation, using relativistic kinematics in the analytical calculation. The simulation results were successfully tested by doing a proton calibration experiment at TANDEM 9MV of IFIN-HH, the maximum relative difference between simulation results and measured points is below 6%.

2.2 Radiochromic films calibration for protons at 9 MV Tandem accelerator

Radiochromic films (RCF) are regularly used as diagnostic tools in laser-plasma experiments, for characterization of the ion beam (mainly protons) generated by laser interactions with different targets [49]. Used as a single film, RCF provides the shape profile of the beam, and, in a stack structure, RCF could resolve the beam energy spectrum from individual energy depositions in each layer.

When irradiated, the RCF active layer undergoes a polymerization reaction [50] having as consequence a colour change. Effectively, the optical density (OD) is changing, the film becoming darker. RCF's are self-developing and are usually scanned with high resolution film scanners. The parameter [51]:

$$OD = \log\left(\frac{PV_{max} - PV_{sig}}{PV_{max} - PV_{bkg}}\right) \quad (6)$$

called optical density is proportional to the deposited dose. It is a function of the pixel values of irradiated (PV_{sig}) and non-irradiated (PV_{bkg}) regions as well as the maximum pixel value (PV_{max}), which is given by the colour depth of the scan [51].

In the future experiments at ELI-NP facility, two types of RCFs are proposed to be used, each corresponding to a specific dose range: HD-V2 with 10 Gy to 1 kGy dose range and MD-V3 with 1 Gy to 100 Gy dose range, both types manufactured by Ashland Inc. USA [52]. In order to provide dose and deposited energy information, the films were calibrated, meaning associating dose to OD values. Even if many data related to the RCF's calibration are given in literature for protons (and by manufacturer for electrons), no universal calibration curve for RCF exists [49]. The reasons are related to different (chemical) changings in the active layer composition, differences from the scanning process, etc. Therefore, it is mandatory for the calibration to be done for the same type of film which will be used in the real experiment, with the same scanner, the same scanning parameters, procedure, etc.

2.2.1 Experimental setup

The experiment for RCF calibration is based on the relation between the RCF response and the scattering cross-section of a proton beam on a Tantalum foil. The protons used are generated by the 9 MV Tandem accelerator of IFIN-HH [53]. The experimental setup is shown in Figure 2.6.

The RCF stack was placed on a circular support, at a distance of 100 mm from the beam-target interaction point, covering angles from 10° to 90° . The support curvature ensured the same distance from the scattering point to the RCF independently of the angle of scattering.

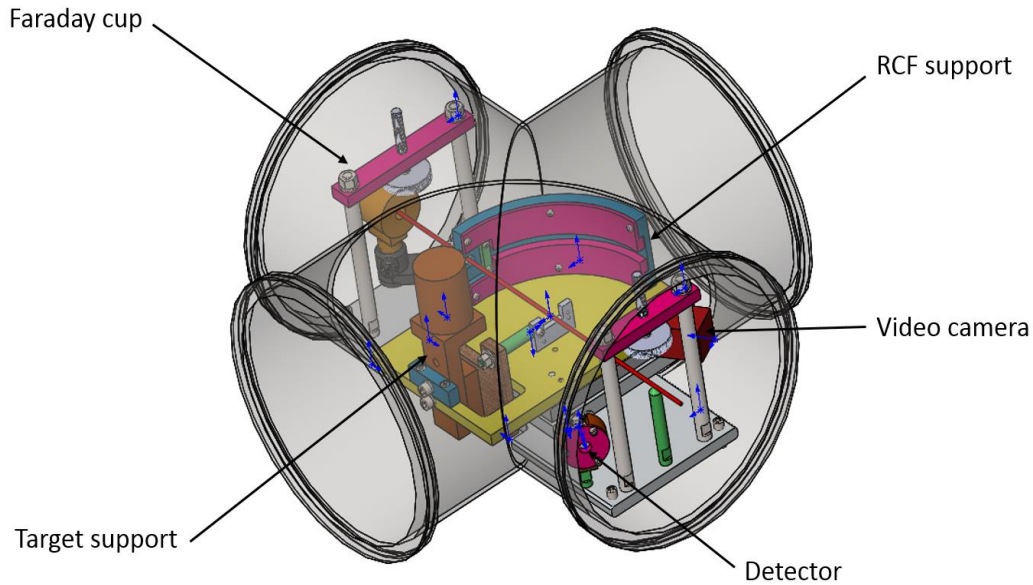


Figure 2.6. RCF calibration experimental setup mounted in the vacuum chamber at IFIN-HH 9MV Tandem accelerator. The proton beam (red line) hits the Tantalum foil and the protons scattered in forward direction irradiate the RCF's, mounted in the curved RCF holder (pink).

2.2.2 Data analysis

The data analysis was presented in [51]. After the irradiation time, each RCF from the stack was scanned in transmission mode, by using a Epson V850 scanner, in 16 bits grayscale at 600 dpi. The grayscale profiles of the irradiated RCF surface (see Figure 2.7) was extracted by using ImageJ image processing software [54] and data analysis was done in ROOT [55].



Figure 2.7: An example of RCF scan image. The irradiated region is placed in the middle side, between two non-irradiated regions. The RCF OD variation (from left to right) is based on the scattering cross-section of a proton beam on a Tantalum foil. The cross-section of the beam inside the target was estimated with the Rutherford formalism for elastic scattering.

The data analysis is based on a grid of angular values starting with 10° , for which the dose was estimated, the OD (according to Eq. 6) and the propagation of the uncertainties were computed as described in the following. The background has been estimated for each RCF image from the non-irradiated regions. The energy depositions of protons in target and RCF layers has been estimated with SRIM [56] and the cross-section of the beam scattering inside the target with the Rutherford formalism for elastic scattering [57].

2.2.2.1 Sources of uncertainty

In the data analysis have been identified several sources of uncertainty associated to both OD and estimated dose. For OD the uncertainty was calculated using the following formula:

$$\delta_{tot}^{OD} = \sqrt{\delta_{aa}^2 + \delta_{bk}^2} \quad (7)$$

and for the estimated dose:

$$\delta_{tot}^{DOS} = \sqrt{\delta_{tt}^2 + \delta_{bd}^2 + \delta_{id}^2} \quad (8)$$

where δ_{xx} are the induced uncertainties for: average scattering angle (aa), background subtraction (bk), target thickness (tt), beam diameter (bd) and integrated dose (id) respectively.

2.2.2.2 Results and discussion

In the analysis the energy deposition in the active layer, the dose and the optical density of each RCF layer in the stack were computed.

In order to deliver functional expressions of the calibration curves, data from all layers for each RCF type were combined, as shown in Figure 2.8. Here, the total dose versus optical density was fitted with a polynomial function:

$$F(OD) = \sum_j a_j OD^j \quad (9)$$

The plots in Figure 2.8 show also the evolution of the RCF response close to saturation and close to the low dose region.

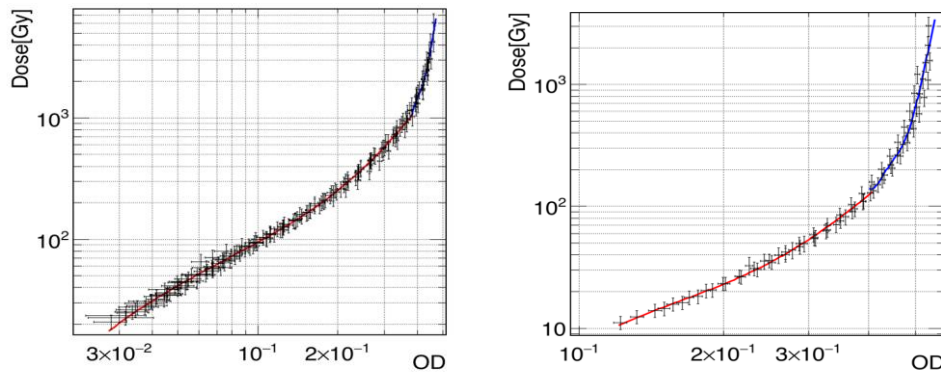


Figure 2.8. Global fits on data from all layers of HD-V2 RCF (left) and MD-V3 RCF (right) stacks.

2.2.3 Proton characterization in LASER acceleration experiments

A stack configuration based on RCF layers can measure the divergence and energy spectrum of protons generated in laser-plasma interactions. Each active layer corresponds to a specific energy of

protons, namely the one given by the Bragg peak. The proton spectrum is deconvoluted with a minimization procedure starting from the deepest layers in the stack. As described in references [49, 58], the total energy deposition in a given RCF layer is the convolution of the spectrum with the RCF response function:

$$E_{tot}(i) = \int_{E'_{min}}^{E'_{max}} \frac{dN(E')}{dE'} E_{dep}(i, E') dE' \quad (10)$$

where dN/dE is the particle number spectrum per unit energy and E_{dep} is the calculated energy loss by a proton with energy E in a given layer i of the stack. E_{dep} can be estimated with a particle propagation code such as SRIM or GEANT 4 [59] for a given stack configuration and E_{tot} for a given layer i is compared with the experimental data in terms of optical density, since E_{tot} is related to the dose, given by Equation 9 in terms of OD. The integral calculates $E_{tot}(i)$ for the interval $[E'_{min}, E'_{max}]$, where E'_{min} is the minimum proton energy necessary for a proton to reach the layer i , and E'_{max} is the maximum energy of a proton which does not escape the layer i . Minimizing the difference between these two quantities one could obtain the expression of the energy spectrum of the laser-accelerated ions, dN/dE . In order to deliver this expression the procedure assumes an *a-priori* behaviour of the proton spectrum; different expressions are presented in [49, 60].

2.2.4 Conclusions

In this chapter we presented a scattering experiment with monoenergetic protons delivered by the 9MV TANDEM electrostatic accelerator at IFIN-HH for the calibration of two RCF types: HD-V2 and MD-V3. As a consequence of the angular dependence of the scattering cross-section of the protons, the setup was able to provide a wide range of doses in a single run. In the analysis of the obtained data, the main systematic uncertainties that influenced the results were considered and the calibration curves were obtained to be used in the reconstruction of the proton beam from laser-plasma experiments in a stack configuration.

Chapter 3

Proton diagnostics based on population and de-excitation of nuclear isomeric states - gamma spectroscopy

In this chapter a method for characterization of laser accelerated proton pulses based on the production in secondary targets of nuclear isomers and in-situ measurement of the γ de-excitation of reaction products using LaBr₃:Ce scintillators is presented. It is in many respects similar to widely used nuclear activation technique such as NATALIE, a system developed at Centre Etudes Nucléaires de Bordeaux Gradignan - CENBG [61], based on β^+ decay and coincidences measurements of the 511 keV gammas following the positron annihilation or NAIS - nuclear activation-based imaging spectroscopy, based on autoradiography of activated foils using IP detectors [62], except that, eliminating the transportation time of the irradiated sample to the gamma detector position, application to high repetition rate laser became possible. Preliminary results are reported in [63, 64] and show that with laser pulses less below PW isomeric states with millisecond lifetimes, and even tents of microseconds with adequate shielding, can be measured.

The feasibility of the method for multi-PW laser pulses is experimentally demonstrated in this thesis by using induced γ de-excitation of the ^{109m}In isomer with energy level $E_{lev}=649.7$ keV and half-live $T_{1/2}=80.4$ s produced in the reaction $^{108...116}\text{Cd} + p \rightarrow ^{109m}\text{In} + xn$, and of the ^{90m}Nb isomer with energy level $E_{lev}=124.7$ keV, $T_{1/2}=18.8$ s, produced in the reaction $^{90...96}\text{Zr} + p \rightarrow ^{90m}\text{Nb} + xn$, at Center for Relativistic Laser Science from Institute for Basic Science - CoReLS/IBS – 4 PW laser facility, Gwangju, South Korea [65, 66]. The ability to measure several isomers simultaneously allows to extract quantitative information on energy and spatial distributions as well as on composition of accelerated proton bunches, if several detectors, placed at various angles, are used simultaneously.

3.1 Method description

This method represents a quasi-online measurement technique which can be used to measure particles produced in high-power laser interaction with a primary target. The accelerated particles interact with a secondary target (or a stack of secondary targets) where they induce nuclear reactions and populate isomeric states [64]. During the de-excitation of the isomeric states of interest delayed γ -rays are emitted and measured in-situ by using detectors with suitable features (a first attempt for in-

situ gamma spectroscopy can be found in [67]). By using these measurements it can be determined the number of particles which hit the secondary target and based on the particles energy loss calculation in the secondary target, can be estimated the particles energy, with tunable resolution, according to the secondary target configuration. The spatial distribution of the particles can be also investigated by using a set-up consisting of several detectors placed around the secondary target (stack of secondary targets), or by placing several targets at various angles.

3.2 Tests and experimental set-up

3.2.1 Detection system – description and characterization

The detection system consists of a $\text{LaBr}_3:\text{Ce}$ scintillator crystal (1.5" diameter x 1.5" height cylinder) coupled to a photomultiplier tube (PMT), connected with a digitizer. The detector assembly was mounted in an air bubble by using a specially designed support (see Figure 3.1).

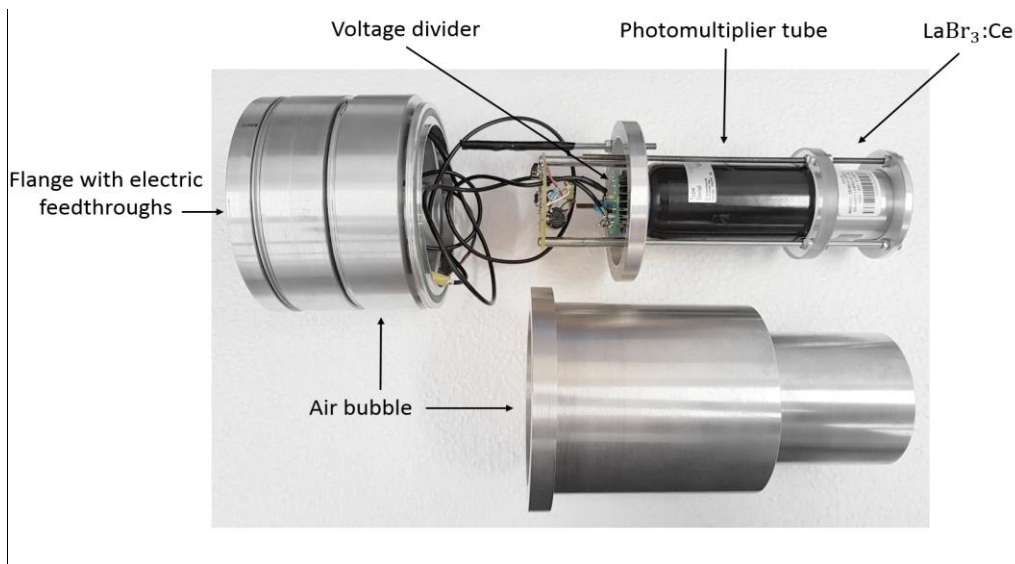


Figure 3.1: The $\text{LaBr}_3:\text{Ce}$ detector assembly. The detector consists of a $\text{LaBr}_3:\text{Ce}$ scintillator crystal (1.5" diameter x 1.5" height cylinder) coupled to a photomultiplier tube (PMT), both mounted in an air bubble.

The air bubble is used to avoid the overheating of the detector electronics (more precisely the voltage divider installed on the PMT inside the air bubble, see Figure 3.1), given that, for this detection technique the detector has to be used in vacuum. The electric signals collected from the detector are converted to a digital signal by using a CAEN digitizer module, its control and data readout by a PC being done with the COMPASS acquisition software [68].

Detector resolution and efficiency

The resolution and efficiency are very important features of a detection system. In order to determine them two standard gamma-ray calibration sources were used, ^{60}Co and ^{152}Eu . The measured gamma peaks were fitted with Gaussian function and relative resolution ($\Delta E_{FWHM}/E_\gamma$) was determined.

It varies between 2.8% at maximum measured energy (1332.5 keV) and 12.4% at minimum measured energy (122 keV).

A key role plays the detector efficiency estimation because determination of the total number of γ -rays emitted from the secondary target is depending on it. In order to determinate with high precision the detector efficiency for each layer of the secondary target (Cd, Al, Zr, with a total thickness of 3.32 mm), we used GEANT4 toolkit.

In addition, to check the simulation accuracy, the measurement using the ^{152}Eu point-like radioactive source ($\Lambda=450.6132$ kBq activity, 1200 s acquisition time) was compared with a GEANT4 simulation, using the same setup. A good agreement was observed, validating the simulation results after applying an overall correction factor of $f=0.846$ to the simulation results supposed to be due to various systematic uncertainties.

3.2.2 Selection of the secondary targets

In the current study the method was applied to diagnose laser accelerated protons. Secondary targets of natural Cd and Zr were used, aiming population of isomeric states in isotopes of In and Nb. The use of natural Cd and Zr ensured the population of a number of nuclear isomeric states, covering a broad range of half-lives and energies of the delayed γ -rays [70].

The proton-induced reactions in a natural Cd ($^{108\dots116}\text{Cd}$) target lead to population of isomeric states in ^{109}In via different reaction channels ($^{108\dots116}\text{Cd} + p \rightarrow ^{109\text{m}}\text{In} + xn$, $E_{lev}=649.7$ keV, $T_{1/2}=80.4$ s). By using the natural Zr ($^{90\dots96}\text{Zr}$) target the 124.7 keV isomeric state in ^{90}Nb can be accessed ($^{90\dots96}\text{Zr} + p \rightarrow ^{90\text{m}}\text{Nb} + xn$, $E_{lev}=124.7$ keV, $T_{1/2}=18.8$ s).

The cross section for above reaction channels were calculated by using TALYS code [69] for a broad range of initial proton energies (0-150 MeV). The decay of all these isomers proceeds through isomeric transition, meaning that there is no competition with beta decay (or electron capture). However not all isomeric states will emit a gamma ray because internal conversion mechanism characterised by the α coefficient [71, 72].

In all mentioned reactions, the atomic number of produced isomers is larger (by 1) compared to the target atomic number such reaction induced by electrons or gamma are excluded.

3.2.3 Experimental set-up

The experimental set-up is shown in Figure 3.2. The laser shots used for this experiment were oriented at 5° incidence angle on the target with respect to the normal incidence. Multi-MeV protons have been produced and impinged on a multi-material secondary target, oriented at 15° incidence angle on the target with respect to the primary target normal incidence.

The secondary target stack had a surface of 50×50 mm² and it was composed by different materials with different thicknesses (1.1 mm Cd, 2 mm Al and 1.22 mm Zr). For proton reactions in Cd

layer, the incident energy threshold is directly related to cross section as function of reaction energy. In case of Zr layer, for the chosen secondary target configuration, the incident energy threshold is 32 MeV as calculated with ATIMA 1.2 stopping power and ranges model [73] implemented in LISE++ [74].

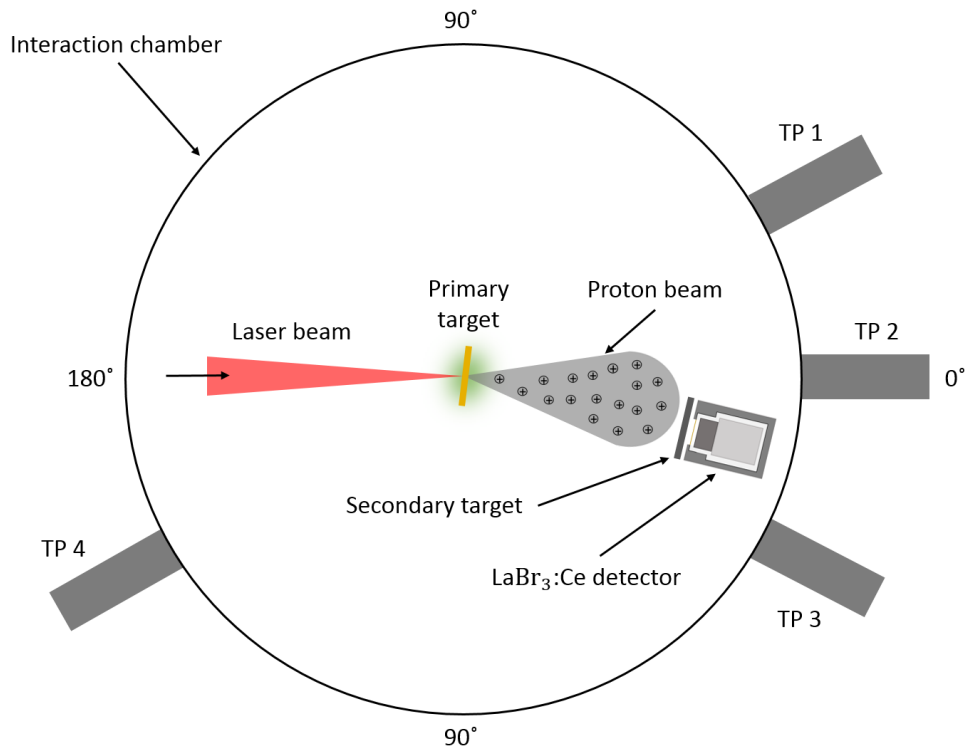


Figure 3.2: Schematic experimental setup used at CoReLS/IBS – 4 PW laser facility. The focalized laser beam (oriented at 5° incidence angle on the target with respect to the normal incidence) hits the primary target, mounted in a multi-target holder. Thomson Parabola (TP) proton spectrometers were installed in forward and backward direction as depicted.

The accelerated protons were characterized in the same shots also in terms energy distribution by using several Thomson Parabola (TP) spectrometers placed at various angles as depicted in Figure 3.2. The secondary target stack was placed at half angle in between the TP2 and TP3 such that the measurements with the two types of diagnostics did not perturb each other. The mean of the maximum proton energies measured for each shot with these two Thomson Parabola spectrometers will be denoted as E_p in the following.

3.3 Measured γ -ray energy spectra – preliminary results

The data analysis was done in ROOT. First thing noticed during the data analysis was the very long recovery time of the detector after certain shots (up to 10 seconds). Also in the case of most shots we noticed a shift of energy as a function of time (see Figure 3.3). These two factors lead to the loss of data associated with short lived isomers. To minimize the time delay between the shot and the useful recorded data we developed in ROOT an algorithm to correct the energy shift in time. The algorithm is

based on the energy curve fitting in the raw bidimensional histogram (see Figure 3.3) and by applying the correction factors to generate a corrected bidimensional histogram (see Figure 3.4). The same algorithm included also the energy calibration, based on 511 keV annihilation peak, and thus the analysis became independent of the setup changes (attenuators, V_{pp} , etc.).

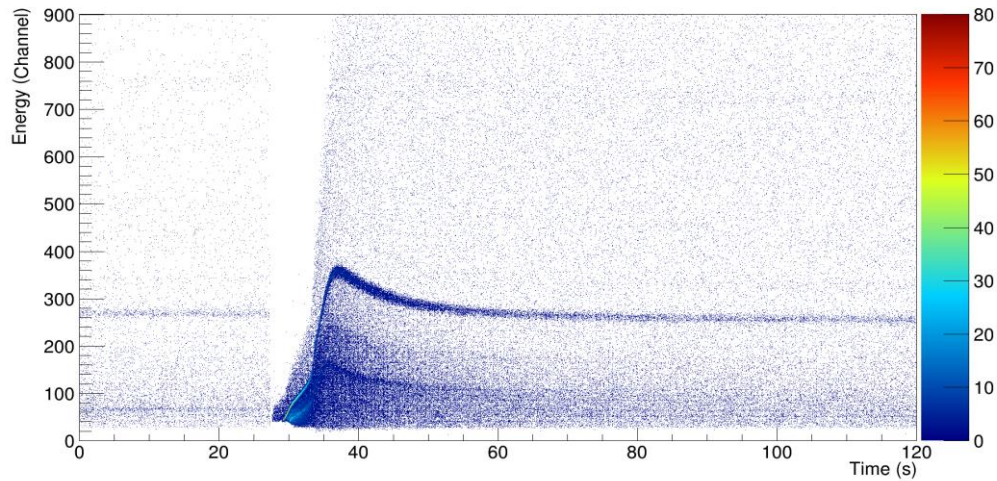


Figure 3.3: Raw bidimensional (Energy, Time) histogram obtained experimentally by using $\text{LaBr}_3:\text{Ce}$ detection system. The distributions show the γ -rays detected in an interval of up to 120 s, before and after the laser shot (shot time: 27.2s)

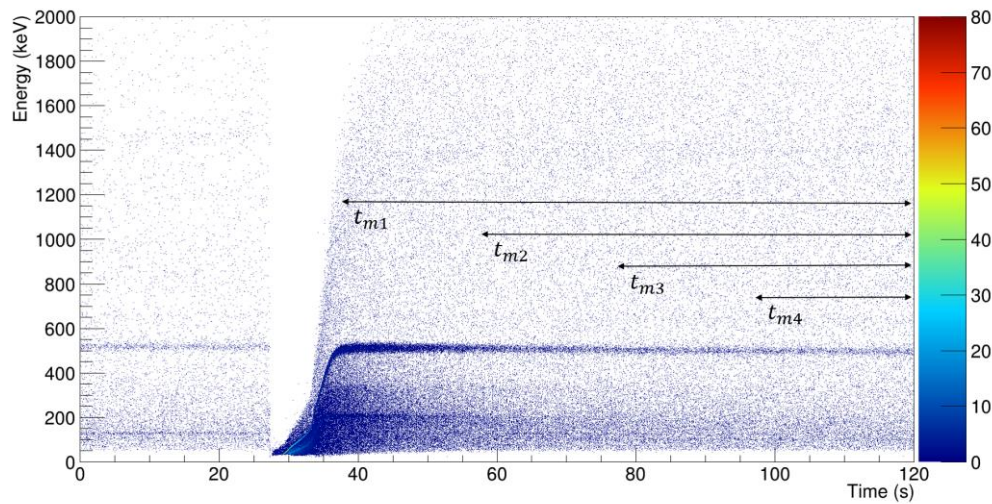


Figure 3.4: Same experimental data as in Figure 3.3 after applying the correction algorithm including also the energy calibration. The arrows indicate the 4 time windows used in data analysis for generation of unidimensional gamma spectra.

To measure the number of detected gamma ray of a certain energy, the projection on y-axis of the bidimensional histograms was done with different integration times (see Figure 3.4). For each shot four projections were done with four different integration time windows t_m . The total number of γ emitted for each isomeric state de-excitation (N_0) was calculated by using the following formula:

$$N_0 = \frac{N_{\gamma m}}{e^{-\frac{\ln(2)}{T_{1/2}} t_{del}} \cdot \left(1 - e^{-\frac{\ln(2)}{T_{1/2}} t_m}\right)} \cdot \left(\frac{1}{\varepsilon^{(det.)}}\right) \quad (11)$$

where $N_{\gamma m}$ is the number of experimentally measured γ counts for an isomeric state populated by a given laser shot, $T_{1/2}$ is the half-life time of the isomer, t_{del} is the delay time from t_0 (shot time) to the point where the measurement starts and t_m is the integration time. $N_{\gamma m}$ is obtained by Gaussian fit with background subtraction in the unidimensional (projected) gamma spectra. By doing the integration on different time intervals the accuracy of the fitting method can be checked. If the peak integration is good and all other parameters are correct, for a given isomer in one shot, the determined γ yield N_0 has to be almost constant, independent of the integration time or the integration starting time, affected only by statistic fluctuations. The number of gamma ray emitted by each isomer was obtained as average of the values obtained for each integration window. Then, the isomer yields have been calculated with relation:

$$Y = N_0^{(av.)} (1 + \alpha) \quad (12)$$

resulting from definition of conversion coefficient α as number of electrons divided by number of gamma rays emitted in the transition. In the Figure 3.5 a gamma spectra is plotted as example.

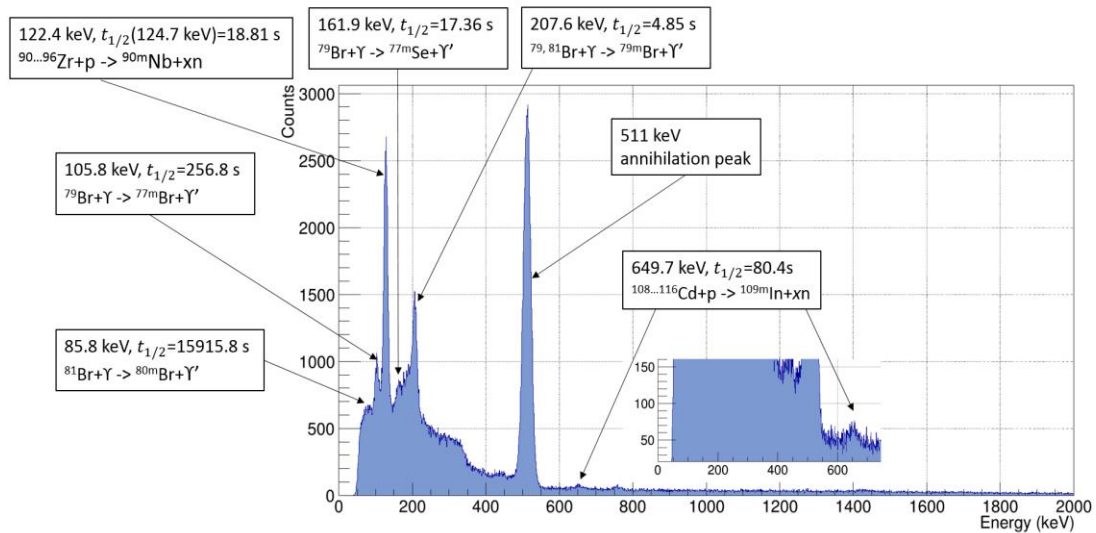


Figure 3.5: Energy spectrum (1 keV bin) obtained experimentally by using LaBr₃:Ce detection system, 100 s integration time, after a single shot. In the spectrum can be observed the gamma-rays following the decay of the isomers populated by proton induced reactions in Zr and Cd and of the isomers populated by γ -induced reactions in Br.

Besides the delayed γ -peaks resulting from the reaction of $^{108,116}\text{Cd} + p \rightarrow ^{109m}\text{In} + xn$, $E_{lev} = 649.7$ keV and $^{90,96}\text{Zr} + p \rightarrow ^{90m}\text{Nb} + xn$, $E_{lev} = 124.7$ keV, other γ -peaks have been observed. After we checked the origin of the unknown γ -peaks we found that a suite of isomers are populated by γ -induced reactions in Br.

Thus, out of the isomers observed in Figure 3.5 we will concentrate in the following on two of them: the ^{109m}In isomer at 649.7 keV produced in Cd foil and ^{90m}Nb at 124.7 keV (and measured through 122.4 keV transition) produced in Zr foil.

During the data analysis we noticed that in the case of the shots where the proton energy E_p was high, for the ^{90m}Nb isomers (124.7 keV) produced in Zr foil, the number of total emitted γ (N_0) is not constant for different integration time t_m (see Figure 3.4). More precisely, it is increasing with the time delay t_{del} . Checking the origin of this problem, we found that if the incident protons have enough energy to reach the LaBr₃:Ce scintillator crystal volume, they populate isomeric states in ^{79}Kr through the reaction $^{79,81}\text{Br} + p \rightarrow ^{79m}\text{Kr} + xn$. The ^{79m}Kr isomer has the excitation energy $E_{lev}=129.8$ keV, thus, overlapping with the ^{90m}Nb γ peak having only 6% less energy compared to 12% energy resolution. The half-life time of the ^{79m}Kr is 50 s, bigger than the half-life time of the ^{90m}Nb which is 18.8 s, this explaining why in this case the N_0 is increasing with the time delay. Based on the cross section values and the secondary target configuration, we calculated that the minimum energy for the incident protons to populate ^{79m}Kr isomeric states to be of ~ 44 MeV.

For the shots with the high measured proton energy E_p we separated the contribution of ^{90m}Nb and ^{79m}Kr isomers by using following procedure based on known decay constants $\lambda^{(1)} = \frac{\ln 2}{T_{1/2}^{(90mNb)}}$ and $\lambda^{(2)} = \frac{\ln 2}{T_{1/2}^{(79mKr)}}$. If we denote with $Y^{(1)}$ the yield (number) of ^{90m}Nb isomers and with $Y^{(2)}$ the yield of ^{79m}Kr isomers, the theoretical number of counts $N_i^{(th.)}$ in the gamma peak corresponding to integration window of duration $t_{m,i}$ starting at time $t_{del,i}$ after the laser shot can be written as the sum

$$N_i^{(th.)} = Y^{(1)}\tilde{a}_i + Y^{(2)}\tilde{b}_i \quad (13)$$

where:

$$\tilde{a}_i = e^{-\lambda^{(1)}t_{del,i}} \left(1 - e^{-\lambda^{(1)}t_{m,i}}\right) \varepsilon^{(1)} = a_i \varepsilon^{(1)} \quad (14)$$

$$\tilde{b}_i = e^{-\lambda^{(2)}t_{del,i}} \left(1 - e^{-\lambda^{(2)}t_{m,i}}\right) \varepsilon^{(2)} = b_i \varepsilon^{(2)} \quad (15)$$

In analogy with relation 11, the factors $\varepsilon^{(1)}$ and $\varepsilon^{(2)}$ are related to detection efficiency but include also the internal conversion efficiency $\alpha^{(1)}$ and $\alpha^{(2)}$, respectively. In case of ^{90m}Nb the gamma efficiency $\varepsilon^{(det.)}$ is given by the calculation from Chapter 3.2.1, while the number of isomers is larger than emitted gamma ray by the factor $(1 + \alpha^{(1)})$. Thus:

$$\varepsilon^{(1)} = \varepsilon^{(det.)} / (1 + \alpha^{(1)}) \quad (16)$$

The situation is more complex in case of ^{79m}Kr isomers because they are decaying from inside scintillator. In order to calculate gamma efficiency in this situation a new set of Monte Carlo simulation by using GEANT4 toolkit have been performed. Additionally, the electrons associated to internal conversion process are depositing their energy in just few tens of micrometres. The very low energy X-

rays accompanying the conversion electrons are also absorbed locally through photoelectric process and, therefore, in case of internal conversion a signal with same amplitude as for the isomeric gamma detection is generated with a detection efficiency of 100%. Consequently, the total efficiency to detect the isomeric decay in the photopeak is in this case the sum of gamma and conversion electron contributions:

$$\varepsilon^{(2)} = \varepsilon / (1 + \alpha^{(2)}) + \alpha^{(2)} / (1 + \alpha^{(2)}) \quad (17)$$

Knowing the a_i and b_i coefficients defined above for the several integration conditions $\{t_{m,i}, t_{del,i}, i = \overline{1, \dots, n}\}$, the two quantities of interest ($Y^{(1)}$ and $Y^{(2)}$) are obtained through the minimization of

$$\chi^2 = \sum_{i=1}^n \frac{(N_i - N_i^{(th.)})^2}{\sigma_i^2} \quad (18)$$

where N_i is the number of counts determined in a Gaussian fit of the gamma peak in the experimental spectrum corresponding to the same integration conditions and σ_i is the associated error as reported by fitting procedure.

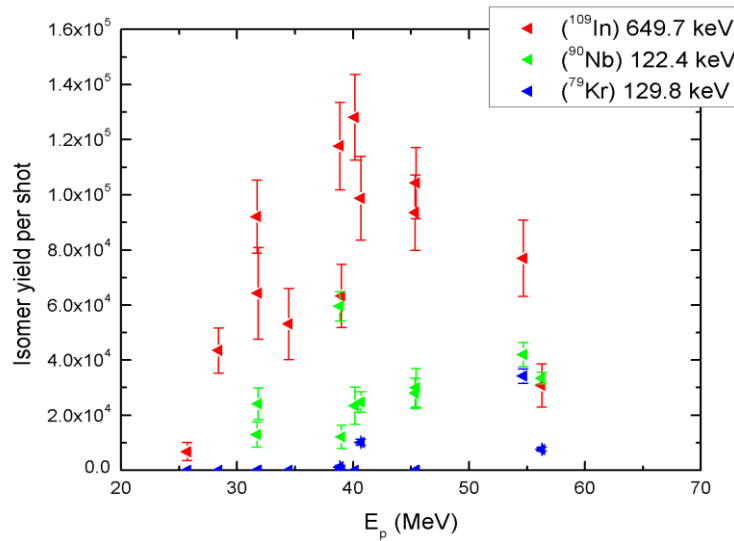


Figure 3.6: The total number of produced ^{109m}In , ^{90m}Nb and ^{79m}Kr isomers as a function of maximum incident proton energy E_p for a number of 13 consecutive shots.

As expected there is no ^{90m}Nb isomers produced for shots with proton energy below 32 MeV. The 44 MeV threshold for production of ^{79m}Kr is less clearly observed, which can be explain by uncertainties in maximum proton energies measured with the two TP spectrometers placed left and right of the detector. The vertical spread of points is also typical for high power laser experiments and it is due to shot-to-shot fluctuation of accelerated proton number and energy spectrum even for the same maximum energy.

3.4 Proton beam characterization

3.4.1 Calculation of the reaction number

The number of reactions in a thin target is calculated with the relation:

$$N = N_{proj} \frac{\rho_{target}}{\mathcal{M}} t_{target} c_{target} N_A \sigma(E_{proj}) \quad (19)$$

where N_{proj} are the number of projectiles, $\sigma(E_{proj})$ is the reaction cross at E_{proj} projectile energy, ρ_{target} , \mathcal{M} , t_{target} , c_{target} are target density, molar mass, thickness and concentration of isotope involved in the considered reaction. Together with Avogadro number, N_A , the factor $\frac{\rho_{target}}{\mathcal{M}} t_{target} c_{target} N_A$ represents the target areal density. The above formula is valid for a very thin target, such that the E_{proj} is constant over target thickness.

In the case of a thick target, if projectile is a charged particle and its energy is decreasing from E_{proj}^{inc} to E_{proj}^{out} , we have to use projectile stopping power $P(E_{proj})$ in the target to get the number.

Neglecting energy and angular straggling phenomena associated to stopping power, we can define the function:

$$E_{proj}(t) = \begin{cases} E_{proj}^{inc} & t = 0 \\ E_{proj}(t) & \\ E_{proj}^{out} & t = t_{target} \end{cases} \quad (20)$$

representing the energy of the projectile at depth t inside target.

So, integrating equation (19) over the target thickness one gets:

$$N = \int_0^{t_{target}} dt N_{proj} C \sigma(E_{proj}(t)) \quad (21)$$

where the following constant is introduced:

$$C = \frac{\rho_{target}}{\mathcal{M}} c_{target} N_A \quad (22)$$

3.4.2 Determination of incident projectile number

The problem we need to solve is the determination of energy distribution of incident particles knowing several measured numbers of reaction (isomer yields) $Y^{(1)}, Y^{(2)}, \dots, Y^{(i)}, \dots, Y^{(k)}$, each corresponding to well-defined experimental conditions in terms of target thickness and composition, as well as knowledge of the involved stopping power $P(E_{proj})$ of the projectile and cross section $\sigma^{(i)}(E_{proj})$ for each reaction type. Obviously, it is not possible to deduce an arbitrary incident

distribution $\mathfrak{D}(E_{proj}^{inc})$ by solving k equations. However, the information embedded in the measured reaction numbers can be used in various approaches, such as:

- a) the $\mathfrak{D}(E_{proj}^{inc})$ is approximated by a function with few parameters that can be obtained in a fit procedure. For example, the ion energy spectrum in TNSA is described in terms of 3 parameters: temperature, energy cut-off and amplitude
- b) a certain range of incident energies can be divided in k bins defined by $\{E_{inc}^j, j = \overline{0, k}\}$ and assumed that the incident distribution has constant $D^{(j)}$ value in each bin. The numbers of reaction of each type can be written:

$$Y^{(i)} = C^{(i)} \sum_{j=1}^{j=k} D^{(j)} F^{(i,j)} \quad (23)$$

where the $F^{(i,j)}$ matrix being defined as:

$$F^{(i,j)} = \int_{E_{inc}^{j-1}}^{E_{inc}^j} dE_{proj}^{inc} \int_{E_{proj}^{out}(E_{proj}^{inc}, t_{target})}^{E_{proj}^{inc}} dE_{proj} \frac{1}{P(E_{proj})} \sigma^{(i)}(E_{proj}) \quad (24)$$

and can be calculated numerically, taking into account, if needed, the layered structure of the target.

Based on the results plotted in Figure 3.6, by using the method b) described above, the proton yield per shot was determined, in three different bins:

- 1) $D^{(1)}$ - from 14 MeV to 32 MeV corresponding to reactions only in Cd layer,
- 2) $D^{(2)}$ - from 32 MeV to 45 MeV corresponding to reactions with high cross section in Zr layer; however, proton with energies in this range will also produce ^{109m}In in Cd foil, but not in scintillator
- 3) $D^{(3)}$ - from 45 MeV to 56 MeV corresponding to reactions also in scintillator, but with lower cross section also in Cd and Zr layers.

The results are shown in Figure 3.7 for the same shots presents in section 3.3. These yields are integrated over the solid angle covered by the detection system which is 9.61×10^{-3} Sr center at 15° relative to incident laser direction. Therefore, they represent only a small fraction of the total protons accelerated in the shot. When divided by solid angle the measured yield, can be observed a good correlation with other results presented in literature (tacking into account the position of the secondary target stack), for laser-driven accelerated proton yields, measured with complementary techniques [3].

The remarkable feature of the data in Figure 3.7 is the decrease of proton yield in the first energy bin when maximal proton energy is above 55 MeV. Taken into account the energy width of each bin, the result suggests a saturation effect of conversion factor from laser energy to proton energies has been reached. That is the higher number of high energy protons not only decrease the number of low energy protons, but also the total number of protons. Obviously, more experimental data is needed to draw a conclusion.

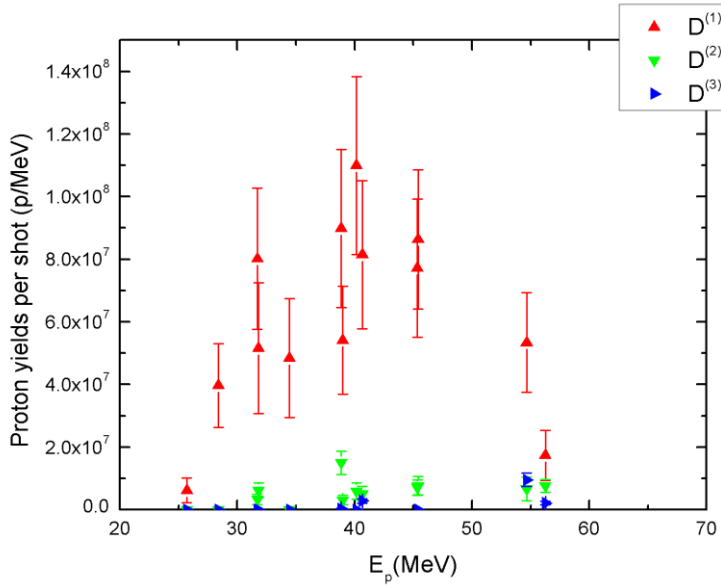


Figure 3.7: The proton yield per shot, in the three bins, $D^{(1)}$, $D^{(2)}$ and $D^{(3)}$ defined in the text, as a function of maximum incident proton energy E_p .

3.5 Detector recovery time

During the data analysis, in case of certain shots (high energy ones) it was observed a very long recovery time of the detector, when the detector is saturated and cannot detect anything, followed by a slow increasing of signal amplitude up to a value above nominal (steady) ones. In some cases the recovery takes even more than 10 seconds (see chapter 3.3, Figures 3.3, 3.4).

To identify the source of the long recovery time of the detector the two major components of the detector, the PMT (coupled with the electronics) and the $\text{LaBr}_3:\text{Ce}$ scintillator crystal [75] were tested.

For the PMT tests an experiment was done by using a 532 nm laser beam with 6 ns pulse duration and the energy ≥ 200 mJ [76]. The results of the tests show that after the PMT receives a strong light flash (170 mJ energy, 6 ns pulse duration), well above its saturation limit, the PMT recovery time is under 1 μs , which indicates that the long recovery time of the detector is not due to PMT.

The $\text{LaBr}_3:\text{Ce}$ scintillator crystal was tested at the ALID 7 [77, 78] electron accelerator from National Institute for Laser, Plasma and Radiation Physics (INFLPR) [79] by using bremsstrahlung radiation, obtained following the interaction of 6 MeV electron beam with a Cu target (5 mm thickness). During the tests a long time light emission of the $\text{LaBr}_3:\text{Ce}$ scintillator crystal, up to 80 μs was recorded. This result is consistent with the study perform in reference [64] were a two exponential fit of the observed afterglow indicated a component of 18 μs decay time and a second component of 266 μs decay time. More detailed study of scintillation mechanisms is reported in reference [80], confirming that the class of scintillator to which $\text{LaBr}_3:\text{Ce}$ belong has, beside the fast component of tens of nanoseconds,

various trapping mechanism of electrons and holes formed in the crystalline structure are responsible for delayed emission.

3.6 Conclusions

In this chapter a method of characterization of laser accelerated proton pulses is presented based on the production in secondary targets of nuclear isomers and in-situ measurement of the γ de-excitation of reaction products, by using LaBr₃:Ce scintillator detectors. It was demonstrated experimentally the method feasibility to measure laser-driven accelerated protons, by using induced γ de-excitation of the $^{110...114}\text{Cd} + \text{p} \rightarrow ^{109...113\text{m}}\text{In} + x\text{n}$, energy level $E_{lev}=649.7$ keV, $T_{1/2}=80.4$ s and $^{90...96}\text{Zr} + \text{p} \rightarrow ^{90\text{m}}\text{Nb} + \text{n}$, energy level $E_{lev}=124.7$ keV, $T_{1/2}=18.8$ s, at CoReLS/IBS – 4 PW laser facility, Gwangju, South Korea. The preliminary results are in a good agreement with what is expected by following the calculations made for the proton energy losses in the secondary target (the thresholds at which the protons reach different states) and of the calculations for the production of isomeric states in the secondary target. In case of the proton yields determined using this method, can be observed a good correlation with other results presented in literature (tacking into account the position of the secondary target stack), for laser-driven accelerated proton yields, measured with complementary techniques.

Outlook and perspectives

This thesis aims to bring contribution to R&D of methods and detectors for characterization of particle pulses generated by high power laser interaction with solid targets. ELI-NP has unique characteristics in this context, it hosts presently the most powerful laser system in the world (2×10 PW) and promises to push the boundaries of knowledge in this area beyond what has been achieved so far. As a consequence, the characterization of the particles accelerated at ELI-NP requires detectors with unique characteristics, not available on the commercial market.

It is known that the interaction of high power laser pulses with solid targets produces in the same time various types of high energy charged particles (protons, ions and electrons) and high intensity electromagnetic fields, ranging from radiofrequency and Terra Hertz range to X-ray and γ ranges. In case of ELI-NP, it is difficult to anticipate precisely the characteristics of radiation and particles generated after the laser interaction with matter and in this thesis extrapolations of known data or results of PIC simulations were used.

Among the methods generally used for detection of laser-driven accelerated particles, the thesis focuses on three of them: particles detection by using TP spectrometers, RCF stacks and a method based on population and de-excitation of nuclear isomeric states.

The TP spectrometers developed in the thesis have unique characteristics. They are designed to measure protons of energy up to 200 MeV and carbon ions of energy up to 160 MeV/n, keeping good energy resolution. Due to the optimized TP spectrometer designs, the energy resolution is below 3% for protons and below 2% for C^{6+} ions, for the whole range of measured energies. The designs were developed based on analytical calculations and SIMION simulations. One of the TP configurations was successfully tested in a calibration experiment at 9MV TANDEM accelerator of IFIN-HH. Beside the theoretical calculations and experiments done for the determination of the particles deflection values and spectrometer resolutions, based on the proton number distribution function of energy for the highest energies obtained so far experimentally and PIC simulations results, the spectrometer signal estimation and calculations for signal to noise ratio (S/N ratio: 7:1) have been done. Based on these calculations the best solution for choosing the resolution/signal ratio and the spectrometers shielding was found, and it was implemented in the spectrometers mechanical design. Further a calibration experiment at 230 MeV Cyclotron Centre Bronowice is proposed.

The second method presented, for laser-driven accelerated particles detection at ELI-NP, is based on RCF stacks. In this part of the thesis a scattering experiment with monoenergetic protons is

presented. The experiment have been done at the 9MV TANDEM accelerator of IFIN-HH, for the calibration of two RCF types: HD-V2 and MD-V3. Even if many data related to the RCFs calibration are given in literature for protons (and by manufacturer for electrons), no universal calibration curve for RCF exists. As a consequence, it is mandatory to perform RCF calibration for the same type of film which will be used in the real experiments at ELI-NP, with the same scanner, the same scanning parameters, procedure, etc. In the analysis of the obtained data, a careful attention was given to the main systematic uncertainties that influenced the results. The calibration curves to be used for a precise reconstruction of the proton beam from laser-plasma experiments in a stack configuration at ELI-NP were determined. The thesis contributes to the development of the method which will be used for proton beam characterisation by using RCF stacks at ELI-NP. Further, based on the acquired expertise a RCF holder and attenuators will be designed and built, for the ELI-NP experiments.

The last method presented in the thesis is based on the production of nuclear isomers in secondary targets and in-situ measurement of the γ de-excitation of reaction products by using $\text{LaBr}_3:\text{Ce}$ detectors. The method feasibility to measure laser-driven accelerated protons, was demonstrated experimentally by using induced γ de-excitation of the $^{110\dots114}\text{Cd} + \text{p} \rightarrow ^{109\dots113\text{m}}\text{In} + xn$, energy level $E_{lev}=649.7$ keV, $T_{1/2}=80.4$ s and $^{90\dots96}\text{Zr} + \text{p} \rightarrow ^{90\text{m}}\text{Nb} + n$, energy level $E_{lev}=124.7$ keV, $T_{1/2}=18.8$ s, at CoReLS/IBS – 4 PW laser facility, Gwangju, South Korea. This method is in many respects similar to the widely used nuclear activation technique such as NATALIE, a system developed at Centre Etudes Nucléaires de Bordeaux Gradignan - CENBG, based on β^+ decay for 511 keV – 511 keV coincidences measurements or NAIS - nuclear activation-based imaging spectroscopy, based on autoradiography of activated foils by using IP detectors, except that, in this case, the gamma detector is placed inside the interaction chamber. This fact eliminates the transportation time of the irradiated sample to the gamma detector position (placed usually outside the interaction chamber), and make this method suitable for high repetition rate measurements. The preliminary results are in a good agreement with what is expected following the calculations made for the proton energy losses in the secondary target and of the calculations for the production of isomeric states in the secondary target. In case of the proton yields determined using this method, can be observed a good correlation with other results presented in literature (tacking into account the position of the secondary target stack), for laser-driven accelerated proton yields, measured with complementary techniques.

Besides the delayed γ -peaks resulting from the de-excitation of ^{109}In ($E_{lev}=649.7$ keV) and ^{90}Nb , ($E_{lev}=124.7$ keV) isomers, produced by proton-induced reactions in Cd and Zr, other γ -peaks have been observed. After the origin of the unknown γ -peaks were checked we found that a suite of isomers are populated by γ -induced reactions in Br. We remark that the population and de-excitation of nuclear γ -induced isomeric states in Br can be used to infer information on the intensity of the γ -rays flash for each shot and also its energy distribution according to the energy threshold of the different γ -induced isomers population in Br. A good correlation between 207.6 keV gamma intensity ($^{79,81}\text{Br} + \gamma \rightarrow ^{79\text{m}}\text{Br} +$

xn) and proton maximum energy E_p measured with TP spectrometers was observed, suggesting a strong link between gamma flash intensity and proton acceleration mechanism.

During the data analysis, in case of certain shots (high energy ones) a very long recovery time of the detector was observed, when the detector is saturated and cannot detect anything, followed by a slow increasing of signal amplitude up to a values above nominal (steady) ones. In some cases the recovery takes even more than 10 seconds. To identify the source of the long recovery time of the detector the two major components of the detector were tested, the PMT (coupled to the electronics) and the LaBr₃:Ce scintillator crystal. In the case of the PMT the results of the tests showed that after the PMT receives a strong light flash, driving it over its saturation limit, the PMT recovery time is under 1 μ s, which indicates that the long recovery time of the detector is not due to PMT. In the case of the LaBr₃:Ce scintillator crystal things are different, as a recovery time of 80 μ s was observed after irradiation with bremsstrahlung radiation obtained by interaction of an electron beam with a Cu target at ALID 7 electron accelerator of INFLPR. This result is consistent with the studies presented in literature, which confirming that the class scintillator to which LaBr₃:Ce belong has, beside the fast component of tens of nanoseconds, various trapping mechanism of electrons and holes formed in the crystalline structure are responsible for delayed emission (up to 1090 s). Tests to investigate this problem will continue, in parallel with the search for solutions to eliminate the long recovery time of the detector.

References

- [1] M. Nishiuchi et al., “Acceleration of highly charged GeV Fe ions from a low-Z substrate by intense femtosecond laser”, *Physics of Plasmas*, **22**, 2015
- [2] F. Wagner et al., “Maximum Proton Energy above 85 MeV from the Relativistic Interaction of Laser Pulses with Micrometer Thick CH₂ Targets”, *Physical Review Letters*, **116**, 2016
- [3] A. Higginson et al., “Near-100 MeV protons via a laser-driven transparency-enhanced hybrid acceleration scheme” *Nature Communications* **9**, 2018
- [4] M. Roth et al., “Bright Laser-Driven Neutron Source Based on the Relativistic Transparency of Solids”, *Physical Review Letters*, **110**, 2013
- [5] I.S. Anderson et al., “Research opportunities with compact accelerator-driven neutron sources”, *Physics Reports*, **654**, 2016
- [6] C. Zulick et al., “Energetic neutron beams generated from femtosecond laser plasma interactions”, *Applied Physics Letters*, **102**, 2013
- [7] Y. Arikawa et al., “Efficient and Repetitive Neutron Generation by Double-Laser-Pulse Driven Photonuclear Reaction”, *Plasma and Fusion Research*, **13**, 2015
- [8] F. Negoita et al. “Laser driven nuclear physics at ELI-NP”, *Romanian Reports in Physics*, **68**, Supplement, P. S37–S144, 2016
- [9] Christopher P. Jones et al., “Evaluating laser-driven Bremsstrahlung radiation sources for imaging and analysis of nuclear waste packages”, *Journal of Hazardous Materials* **318**, 2016
- [10] Silvia C. et al., “Gamma-rays from harmonically resonant betatron oscillations in a plasma wake”, *Nature Physics*, **7**, 2011
- [11] S. Chen et al., “MeV-Energy X Rays from Inverse Compton Scattering with Laser-Wakefield Accelerated Electrons”, *Physical Review Letters*, **110**, 2013
- [12] M. Bobeica et al., “Radioisotope production for medical applications at ELI-NP”, *Romanian Reports in Physics*, **68**, Supplement, P. S847–S883, 2016
- [13] T. Asavei et al., “Materials in extreme environments for energy, accelerators and space applications at ELI-NP”, *Romanian Reports in Physics*, **68**, Supplement, P. S275–S347, 2016
- [14] J.C. Fernández et al., “Fast ignition with laser-driven proton and ion beams”, *International Atomic Energy Agency Nuclear Fusion Nucl. Fusion*, **54**, 2014
- [15] <http://www.eli-np.ro>
- [16] P. Gibbon et al., “Short Pulse Laser Interaction with Matter, An Introduction”, Imperial College Press, 2015

- [17] A. Macchi et al, “Ion acceleration by superintense laser-plasma interaction”, *Rev. Mod. Phys.*, **85**, 2013
- [18] A. Macchi et al., “A Review of Laser-Plasma Ion Acceleration”, arXiv:1712.06443v1 [physics.plasm-ph], 2017
- [19] S. C. Wilks et al., “Energetic proton generation in ultra-intense laser–solid interactions”, *Physics of Plasmas*, **8**, 542, 2001
- [20] K. A. Tanaka et al., “Current status and highlights of the ELI-NP research program”, *Matter Radiat. Extremes*, **5**, 2020
- [21] S. A. Gaillard et al., “Increased laser-accelerated proton energies via direct laser-light-pressure acceleration of electrons in microcone targets”, *Phys. Plasmas*, **18**, 2011
- [22] A. Henig et al., “Radiation-Pressure Acceleration of Ion Beams Driven by Circularly Polarized Laser Pulses”, *Physical Review Letters*, **103**, 2009
- [23] D. Gwynne et al., “Modified Thomson spectrometer design for high energy, multi-species ion sources”, *Review of Scientific Instruments*, **85**, 2014
- [24] D. Jung et al., “Development of a high resolution and high dispersion Thomson parabola”, *Review of Scientific Instruments*, **82**, 2011
- [25] J.J. Thomson “Rays of positive electricity”, *Phil Mag*, S. 6, No 122, 21, 1911
- [26] R. Prasad et al., “Calibration of Thomson parabola—MCP assembly for multi-MeV ion spectroscopy”, *Nuclear Instruments and Methods in Physics Research A*, 623, 2010
- [27] P. Bolton et al., “Instrumentation for diagnostics and control of laser-accelerated proton (ion) Beams”, *Physica Medica*, October, 2013
- [28] L. Torrisi et al., “Compact Thomson parabola spectrometer for fast diagnostics of different intensity laser-generated plasmas”, *PHYSICAL REVIEW ACCELERATORS AND BEAMS*, **22**, 2019
- [29] F. Schillaci et al., “Calibration and energy resolution study of a high dispersive power Thomson Parabola Spectrometer with monochromatic proton beams”, *Journal of Instrumentation*, **9**, 2014
- [30] P. G. A. Cirrone et al., “A new Thomson Spectrometer for high energy laser-driven beams diagnostic”, *Journal of Instrumentation*, **9**, 2014
- [31] K. Michel et al., “Development and calibration of a Thomson parabola with microchannel plate for the detection of laser-accelerated MeV ions”, **79**, 2008
- [32] S. Gales et al., “The extreme light infrastructure-nuclear physics (ELI-NP) facility: new horizons in physics with 10 PW ultra-intense lasers and 20 MeV brilliant gamma beams”, *Rep. Prog. Phys.*, **81**, 2018
- [33] D. Ursescu et al., “Laser Beam Delivery at ELI-NP”, *Romanian Reports in Physics*, Vol. 68, Supplement, P. S11–S36, 2016
- [34] <https://simion.com>
- [35] M. J. Mead et. al., “Electromagnetic pulse generation within a petawatt laser target chamber”, *Review of Scientific Instruments*, no. 10, 75, 2004

- [36] F. Consoli et al., “Laser produced electromagnetic pulses: generation, detection and mitigation”, *High Power Laser Science and Engineering*, 8, 2020
- [37] A. Mančić et al., “Absolute calibration of photostimulable image plate detectors used as (0.5-20 MeV) high- energy proton detectors”, *Review of Scientific Instruments*, **79**, 2008
- [38] A. Alejo et al., “High resolution Thomson Parabola Spectrometer for full spectral capture of multi-species ion beams”, *Review of Scientific Instruments*, **87**, 2016
- [39] J. Teng et al., “A compact high resolution Thomson parabola spectrometer based on Halbach dipole magnets”, *Nuclear Inst. and Methods in Physics Research, A* **935**, 2019
- [40] J. A. Cobble et al., “High-resolution Thomson parabola for ion analysis”, *Review of Scientific Instruments*, 82, 2011
- [41] N. Sinenian et al., “The response of CR-39 nuclear track detector to 1–9 MeV protons”, *Review of Scientific Instruments*, 82, 2011
- [42] <https://www.carestream.com>
- [43] C. G. Freeman et al., “Calibration of a Thomson parabola ion spectrometer and Fujifilm imaging plate detectors for protons, deuterons, and alpha particles”, *Review of Scientific Instruments*, **82**, 2011
- [44] L. Tudor et al., “The design of a proton spectrometer for 60-200 MeV energy range”, *U.P.B. Scientific Bulletin Series A*, **79**, Iss. 4, 2017
- [45] Helmuth S., “Introduction to Radiation Detectors and Electronics”, 1999
- [46] K. Nakamura et al., “Electron beam charge diagnostics for laser plasma accelerators”, *Physical Review Special Topics–Accelerators and Beams*, **14**, 2011
- [47] <https://www.schott.com>
- [48] <https://www.pco.de>
- [49] F. Nürnberg et al., “Radiochromic film imaging spectroscopy of laser-accelerated proton beams”, *Review of Scientific Instruments*, **80**, 2009
- [50] W. McLaughlin et al., “Radiochromic Solid State Polymerization Reaction, Irradiation of Polymers, American Chemical Society”, 1996
- [51] A. S. Cucoanes et al., “Radiochromic film calibration at 9 MV accelerator of IFIN-HH”, *Proceedings of the Romanian Academy, Series A*, **20**, 2019
- [52] <https://www.ashland.com/products/gafchromic-radiotherapy-films>
- [53] D. G. Ghita et al., “Improvements of the research infrastructure at the tandem laboratory in IFIN-HH”, *AIP Conf. Proc.* 1525, **208**, 2013
- [54] W. S. Rasband, “ImageJ, U.S. National Institutes of Health, Bethesda, Maryland, USA”. See also: <https://imagej.nih.gov/ij/>
- [55] R. Brunand et al., “ROOT-An Object Oriented Data Analysis Framework, Proceedings AIHENP’96 Workshop, Lausanne”, 1996, *Nucl. Inst. & Meth. in Phys. Res. A* **389**, 1997. See also <http://root.cern.ch>
- [56] J. F. Ziegler et al., “SRIM-The stopping and range of ions in matter”, *Nucl. Inst. and Meth. in Phys. Res. B* **268**, 2010

- [57] J. W. Mayer et al., “Ion Beam Handbook for Material Analysis, Academic Press, New York”, 1977
- [58] M. Schollmeier et al., “Improved spectral data unfolding for radiochromic film imaging spectroscopy of laser-accelerated proton beams”, *Rev. of Sci. Instr.* **85**, 2014
- [59] S. Agostinelli et al., “Geant4 - a simulation toolkit”, *Nucl. Inst. & Meth. In Phys. Res. A*, **506**, 2003
- [60] J. Fuchs et al., “Laser-driven proton scaling laws and new paths towards energy increase”, *Nature Physics*, **2**, 2006
- [61] M. Tarisien et al., “NATALIE: A 32 detector integrated acquisition system to characterize laser produced energetic particles with nuclear techniques”, *Review of Scientific Instruments*, **82**, 2011
- [62] M. M. Günther et al. “NAIS: Nuclear activation-based imaging spectroscopy” *Review of Scientific Instruments*, **84**, 2013
- [63] F. Negoita et al., “Perspectives for neutron and gamma spectroscopy in high power laser driven experiments at ELI-NP”, *AIP Conference Proceedings*, **1645**, 2015
- [64] M. Tarisien et al., “Scintillators in High-Power Laser-Driven Experiments” *IEEE Transactions on Nuclear Science*, **65**, no. 8, 2018
- [65] J. H. Sung et al., “0.1 Hz 1.0 PW Ti:sapphire laser”, *Optics Letters*, **35**, 2010
- [66] J. H. Sung et al., “4.2 PW, 20 fs Ti:sapphire laser at 0.1 Hz”, *Optics Letters*, **42**, 2017
- [67] R. J. Clarke et al., “Detection of short lived radioisotopes as a fast diagnostic for intense laser-solid Interactions”, *Applied Physics Letters*, **89**, 2006
- [68] <https://www.caen.it>
- [69] A. J. Koning et al., “Proceedings of the International Conference on Nuclear Data for Science and Technology” **211**, 2008
- [70] <https://www.nndc.bnl.gov>
- [71] <http://bricc.anu.edu.au/index.php>
- [72] T. Kibédi, et al., “Evaluation of theoretical conversion coefficients using BrIcc' *Nucl. Instr. and Meth. A*” **589**, 2008
- [73] <http://web-docs.gsi.de/~weick/atima>
- [74] <http://lise.nscl.msu.edu>
- [75] <https://www.crystals.saint-gobain.com/products/standard-and-enhanced-lanthanum-bromide>
- [76] <https://www.quantel-laser.com/en/products/item/q-smart-450-mj-.html>
- [77] D. Ticoş et al., “Complementary dosimetry for a 6 MeV electron beam”, *Results in Physics*, **14**, 2019
- [78] http://ale.inflpr.ro/index_files/Facilitati.htm
- [79] <http://www.inflpr.ro>
- [80] O. Sellès, “Halogénures de lanthane dopés cérium Des scintillateurs rapides pour l'imagerie médicale,” Ph.D. dissertation, Dept. ENSCP, Univ. Paris VI, Paris, France, 2006

Peer reviewed publications

1. K. A. Tanaka , K. M. Spohr , D. L. Balabanski , S. Balascuta , L. Capponi , M. O. Cernaianu , M. Cuciuc , A. Cucoanes , I. Dancus , A. Dhal , B. Diaconescu , D. Doria , P. Ghenuche , D. G. Ghita , S. Kisyov , V. Nastasa , J. F. Ong , F. Rotaru , D. Sangwan , P.-A. Söderström, D. Stutman , G. Suliman , O. Tesileanu , **L. Tudor** , N. Tsoneva , C. A. Ur , D. Ursescu , and N. V. Zamfir, “Current status and highlights of the ELI-NP research program”, *Matter Radiat. Extremes* **5**, 024402, 2020;
2. A. S. Cucoanes, M. Gugiu, F. Rotaru, F. Negoita, **L. Tudor**, S. Kisyov, C. Manailescu, V. Nastasa, “RADIOCHROMIC FILM CALIBRATION AT 9 MV ACCELERATOR OF IFIN-HH”, *PROCEEDINGS OF THE ROMANIAN ACADEMY, Series A, Volume 20, Number 1/2019*, pp. 29–36, 2019;
3. M. Tarisien , J. L. Henares, C. Baccou, T. Bonnet, F. Boulay, F. Gobet, M. Gugiu, F. Hannachi, S. Kisyov, C. Manailescu, V. Meot, F. Negoita, X. Raymond, G. Revet, **L. Tudor**, M. Versteegen “Scintillators in High-Power Laser-Driven Experiments”, *“IEEE TRANSACTIONS ON NUCLEAR SCIENCE, VOL. 65, NO. 8, 2018*
4. **L. Tudor**, F. Negoita, D. Stutman, C. A. Ur, M. Gugiu, A. Cucoanes, F. Rotaru, C. Manailescu, S. Kisyov, “The design of a Proton Spectrometer for 60-200 MeV energy range”, *U.P.B. Sci. Bull. Series A, Vol. 79, Iss. 4, 2017*

Acknowledgements

I want to thank all my colleagues and collaborators who supported me throughout the doctoral thesis period, without whom I would not have been able to reach this point.

First of all, I would like to thank my coordinator, Dr. Călin A. Ur, who offered me the opportunity to study and develop professionally and personally at Extreme Light Infrastructure Nuclear Physics (ELI-NP), the facility that currently hosts the most powerful laser in the world.

Special thanks to Dr. Florin Negoită, who guided me carefully throughout the doctoral thesis period and supported me with everything I needed.

I am also grateful to Dr. Il Woo Choi and the facility members involved, for the support offered during the experiment performed at Center for Relativistic Laser Science from Institute for Basic Science - CoReLS/IBS – 4 PW laser facility, Gwangju, South Korea.

Many thanks to Dr. Călălin Ticoș for the opportunity offered to use the ALID 7 electron accelerator from National Institute for Laser, Plasma and Radiation Physics (INFLPR).

Also I would like to thank to my colleague Eng. Matei Tătaru for the engineering support and the CAD designs presented in the thesis.

Last but not least, I want to thank my colleagues Dr. Stanimir Kisiov, Dr. Pär-Anders Söderström, Dr. Florin Rotaru, Dr. Marius M. Gugiu and Dr. Andi S. Cucoaneș, with whom I participated in several experiments and also answered all the questions I had.

The work reported in the thesis was supported by the Project Extreme Light Infrastructure Nuclear Physics (ELI-NP) Phases I and II, a project co-financed by the Romanian Government and European Union through the European Regional Development Fund.